

Cite this: DOI: 00.0000/xxxxxxxxxx

Molecular Dynamics Simulation of the Coalescence of Surfactant-Laden Droplets[†]Soheil Arbabi,^a Piotr Deuar,^a Mateusz Denys,^a Rachid Bennacer,^b Zhizhao Che,^c and Panagiotis E. Theodorakis^{*a}

Received Date

Accepted Date

DOI: 00.0000/xxxxxxxxxx

We investigate the coalescence of surfactant-laden water droplets by using several different surfactant types and a wide range of concentrations by means of a coarse-grained model obtained by the statistical associating fluid theory. Our results demonstrate in detail a universal mass transport mechanism of surfactant across many concentrations and several surfactant types during the process. Coalescence initiation is seen to occur via a single pinch due to aggregation of surface surfactant, and its remnants tend to become engulfed in part inside the forming bridge. Across the board we confirm the existence of an initial thermal regime with constant bridge width followed by a later inertial regime with bridge width scaling roughly as the square root of time, but see no evidence of an intermediate viscous regime. Coalescence becomes slower as surfactant concentration grows, and we see evidence of the appearance of a further slowdown of a different nature for several times the critical concentration. We anticipate that our results provide further insights in the mechanisms of coalescence of surfactant-laden droplets.

1 Introduction

While ubiquitous in nature, droplet coalescence is also an important process in various industrial applications, where the rate of coalescence can determine their performance. For example, in the context of bio-related microfluidic technologies, slowing down coalescence in bio-particle encapsulation on lab-on-chip devices is often desirable, and can be achieved by using various additives, such as surfactants.^{1,2} In contrast, speeding up the rate of coalescence by adding surfactant could be advantageous in applications, such as coatings³ and superspreading.^{4,5}

Experimental, theoretical, and numerical studies of coalescing droplets have thus far mainly focused on cases without additives, *e.g.* water or polymer droplets.^{6–30} From

the point of view of numerical simulations, these have by and large provided descriptions of the macroscopic and dynamic properties of coalescence,^{7,8,20–22,31–33} but they generally continue to suffer from inadequate resolution at the pinching point between droplets at the initial stage of coalescence, despite progress in this area.¹² Moreover, a detailed molecular-level description of the mass transport mechanism of surfactant is beyond the reach of any continuum model.^{10,34}

Various attempts have been made to tackle this challenge. For example, numerical models based on advection–diffusion equations and chemical kinetic fluxes attempt to incorporate the mass transport of surfactant into the equations,³⁵ but these are only as good as the assumptions put into the model, while a detailed molecular description still remains out of reach for continuum simulation. When it comes to experimental techniques,^{34,36–44} high-speed imaging and particle-image velocimetry have been applied in investigating coalescence of surfactant-laden droplets, and have mainly focused on the macroscopic description of this phenomenon, much as in the case of numerical simulation. Due to device limitations, capturing with high res-

^a Institute of Physics, Polish Academy of Sciences, Al. Lotników 32/46, 02-668 Warsaw, Poland.

^b Université Paris-Saclay, CentraleSupélec, ENS Paris-Saclay, CNRS, LMPS - Laboratoire de Mécanique Paris-Saclay, 91190, Gif-sur-Yvette, France

^c State Key Laboratory of Engines, Tianjin University, 300350 Tianjin, China.

[†] Electronic Supplementary Information (ESI) available: [details of any supplementary information available should be included here]. See DOI: 10.1039/cXsm00000x/

olution the early stages of coalescence during experiments poses a major challenge. Both experiments and continuum modelling are unable to provide a detailed description of the mass transport mechanism at the molecular level. In the case of molecular simulations, all-atom molecular dynamics (MD) has explained different microscopic aspects of coalescence, such as the role of the capillary waves on droplets' surface, but these have only been in the context of pure water droplets,⁹ except for one recent study which considered a few cases.⁴⁵

On the whole, though, the effect of surfactant in droplet coalescence has largely remained unexplored, with implications actually reaching beyond this, for example, in the context of surfactant-laden coalescence between micelle and bilayer⁴⁶. The initial work⁴⁵ suggests that it plays an important role, *e.g.* affecting the coalescence rate and dampening internal droplet dynamics. Reduction of the surface tension at the liquid–gas (LG) interface is usually expected, but the type of surfactant (*e.g.*, chemical groups and molecular architecture) and its concentration are also anticipated to differently affect the coalescence process. Differences are expected even when the concentration is higher than the critical aggregation concentration (CAC) and surface tension at the LG interface is expected to remain constant.^{47–51} On that account, unveiling the details of this phenomenon from a molecular-level perspective is key for fundamentally understanding the underlying mechanisms that can lead to tailor-made surfactant designs for applications.

Here we report on a more detailed and robust study of droplet coalescence using the methods of Ref. 45, and a broader range of surfactants and their concentrations. We employed a high-fidelity coarse-grained force-field enabling us to simulate with MD the coalescence of surfactant-laden droplets. We discuss the details of coalescence at each stage of the process by comparing systems with different surfactant type and concentration. Our data indicate that the underlying mechanisms of coalescence are consistent between the different cases, which point to universal features of surfactant transport and droplet dynamics for the coalescence of water droplets with surfactant. Differences in the behaviour of different surfactants are also highlighted when relevant. The dynamic and static characteristics are unveiled by discussing both macroscopic- and molecular-level quantities, such as the bridge growth dynamics and the velocity of droplet approach, as well as describing the molecular transport of surfactant within the liquid phase. Thus, we anticipate that the present study lays a comprehensive account of the coalescence of surfactant-laden droplets.

In the following section, we provide background infor-

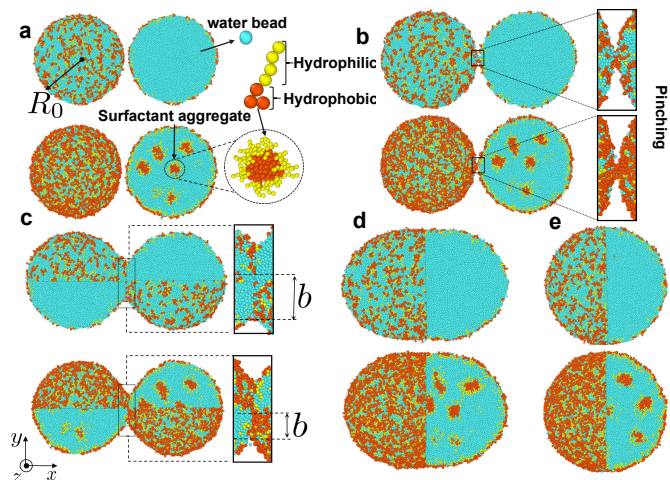


Fig. 1 Coalescence of droplets with C10E4 surfactant at low concentration (6.25 wt%, top of each panel) below CAC = 7.5 wt% and concentrations above CAC (24.18 wt%, bottom of each panel). Snapshots show the initial approach of the droplets (a), their pinching and initial formation of the bridge (b), see also ESI for a movie showing the pinching of the droplets), configurations with a partially (c) and fully (d) developed bridge, and the final equilibrium state (e). External or cross-section views are shown to highlight the bulk, surface, and bridge structure of the droplets. Magnified views of a micelle, a surfactant molecule, and a water bead are shown in panel (a). Water vapour surrounding the droplets is not shown for the sake of clarity.

mation for droplet coalescence. Then, Section 3 gives details on our model and methodology, while Section 4 presents and discusses the results of the coalescence simulations. Section 5, draws some broader conclusions.

2 Background

A macroscopic description of the droplet coalescence can generally be divided into three stages (see Fig. 1). The approach of the droplets, which leads to the initiation of the phenomenon (pinching) as a result of the inter-molecular interactions; the subsequent growth of the bridge formed between the droplets; and the final stage towards equilibrium, which manifests itself by the formation of a single spherical droplet. The system is driven towards the equilibrium state as it seeks to minimise the free-energy associated with the surface tension at the droplet boundary. Hence, on the coarsest level, the formation of larger droplets is energetically favourable. In particular, for a droplet with N beads, the droplet radius behaves as $R_0 \propto N^{1/3}$ (Fig. 1a) since the volume scales as N , while surface tension force as $\propto N^{2/3}$.

The rate of bridge growth after the initial contact is key for characterising the coalescence process and can generally be described from the point of view of fluid dynam-

ics by two successive regimes, namely the viscous regime (VR) and the inertial regime (IR).^{6,52} Moreover, recent MD simulations have uncovered the existence of a third, thermal regime (TR) during the droplet pinching at the very initial stage of the coalescence process,^{9,45} which will be discussed later in more detail. The characteristic velocity in the VR can be defined as $v_v = \gamma/\eta$, where γ is the surface tension and η the viscosity, which suggests that the capillary number $Ca = \eta v_v/\gamma \sim 1$, with the characteristic time scale for droplet-sized effects being $t_v = R_0\eta/\gamma^{10}$, with R_0 the droplet radius as in Fig. 1. As coalescence proceeds to the subsequent IR, the bridge flow can be characterised by the Weber number, namely $We = \rho v_i^2 R_0/\gamma \sim 1$ indicating the limit that inertia effects will take over the surface tension effects, while ρ is the density of the fluid. The bridge velocity is found to scale as $v_i \sim \sqrt{\gamma/\rho R_0}$, and thus the characteristic time scale is $t_i = \sqrt{\rho R_0^3/\gamma}$. For many purposes, especially in the VR, the more relevant length scale is the radius of the bridge, b (Fig. 1), and the corresponding Reynolds number can be defined as $Re = \rho v b/\eta$, which in the VR is $\rho \gamma b/\eta^2$. On the one hand, since the bridge radius is very small in the initial stage, the viscous forces are dominant regardless of the values of γ and η and $Re \ll 1$. On the other hand, $Re \geq 1$ reflects the IR.⁵³ Hence, it can be taken that the crossover between the viscous and the inertial regimes would take place for $Ca \sim 1$ or $Re \sim 1$. Taking the IR expression $v_i \sim \sqrt{\gamma/b\rho}$ using bridge size, we obtain an estimate of the crossover bridge-radius, $b_c = \eta^2/\rho\gamma$, and a characteristic time $t_c = \eta^3/\rho\gamma^2$, which for water droplets would roughly correspond to $b_c \sim 15$ nm and $t_c = 0.1$ ns, highlighting the fast time scales of coalescence.¹¹

In the VR, where inter-molecular forces are playing a dominant role in pulling the droplets together, a linear scaling has been proposed for the growth of the bridge radius with time, *i.e.* $b \propto t$, as well as logarithmic corrections, $b \propto t \ln t$.^{10,34} In the case of the IR, a power-law scaling law has been suggested for the bridge, namely $b \propto \sqrt{t}$.^{10,34} Experimental studies on the coalescence of water droplets are consistent with this and have shown that 0.7 ns after the first contact of the droplets, drag forces give way to the inertial ones and the bridge radius has been reported to scale with time as $b \propto (R_0\gamma/\rho)^{1/4} t^{1/2}$ where R_0 is the initial droplet radius.^{10–12,53,54} Other works have proposed scaling regimes that depend on the ratio of characteristic scales to the viscous length scale $l_v = \eta^2/\rho\gamma$.^{52,55} Moreover, it is argued that the inertia of the droplets cannot be neglected at the initial stage of coalescence. Then, the initial stage would be better described as inertially limited viscous (ILV) regime and a linear scaling with time for the bridge radius has been proposed, which, according to numerical

simulations, is only realised when the coalescing drops are initially separated by a finite distance.²⁰ In the case of miscible and immiscible droplets, a similar viscous dominated regime has been suggested, but immiscible droplets seem to develop a bridge slower.⁵⁶

All-atom molecular dynamics simulations of pure two-dimensional (cylindrical) water droplets have found that multiple precursor bridges develop via thermal fluctuations at the droplet's surface, which initially connect the droplets and then grow, thus identifying a thermal regime at the onset of coalescence.⁹ After a certain threshold, when the radius of the growing bridge becomes larger than a thermal length scale, $l_T \approx (k_B T/\gamma)^{1/4} R_0^{1/2}$, the hydrodynamic regime is recovered, continuum models can describe the process, and one expects VR, IR, or ILV scaling. k_B is Boltzmann's constant and T the temperature. Since surface tension appears in the denominator, the addition of surfactant, which lowers the surface tension, is expected to lead to the increase of the thermal length, l_T , towards an upper limit that is attained above the CAC. Moreover, these all-atom MD simulations have found that, in the TR, the bridge radius expands linearly in time with a velocity much faster than the viscous–capillary regime due to the thermal, molecular ‘jumps’ at the droplets’ surface where multiple bridges are formed.⁹ The initial thermal regime has also been recently observed in the case of coarse-grained models for pure and surfactant-laden three-dimensional (spherical) droplets, without the formation of multiple thermal bridges but a single pinching point instead.⁴⁵

The above considerations indicate that coalescence is still under intensive debate even in the case of pure water droplets. Moreover, only a few studies have dealt with droplet coalescence in the presence of surfactant.^{36–38,40–44,57–66} While it is generally expected that surfactant would decrease the surface tension of the droplets and a delay in the process would be potentially forecast,^{39,61} comprehensive understanding is currently lacking, which calls for a systematic investigation of different surfactants for a range of concentrations. It has been experimentally shown that the presence of surfactant would locally reduce the surface tension on the droplet surface and a nonuniform surfactant concentration would lead to surface tension gradients that would eventually lead to surface flow (Marangoni flow) and a rearrangement of the surfactant molecules to counteract the gradient would delay the coalescence process.³⁶ One might also attempt to see whether the diffusion and adsorption of surfactant at the droplets’ LG interface would further affect the coalescence process, for example, by influencing the flow field of the water molecules,⁴⁵ especially when surfactant concentration is above the CAC and surfactant aggregates are

present in large amounts within the liquid bulk. MD simulations based on a high-fidelity coarse-grained force-field are capable of addressing these and other questions.

3 Model and Methods

An important motivation for choosing the force-field for the problem at hand is the ability to simulate relatively large droplets that could allow for the investigation of the surfactant mass transport mechanism with MD. Based on the fact that coarse-grained force-fields would be a natural choice in this case, and our success in previous investigations on the mass transport mechanism of surfactant in the context of the superspreading phenomenon,^{4,5,67–69} we have embarked on carrying out our studies here by using MD simulations based on the SAFT (statistical associating fluid theory) force-field.^{70–75} More specifically, a force-field based on the SAFT- γ Mie theory⁷⁶ is used, which can accurately reproduce relevant key properties of water-surfactant systems, such as their phase behaviour and surface tension.^{5,67,77–79}

In the case of the SAFT force-field, interactions between different coarse-grained (CG) beads within a distance smaller than r_c are described via the Mie potential, which is mathematically expressed as

$$U(r_{ij}) = C\epsilon_{ij} \left[\left(\frac{\sigma_{ij}}{r_{ij}} \right)^{\lambda_{ij}^r} - \left(\frac{\sigma_{ij}}{r_{ij}} \right)^{\lambda_{ij}^a} \right], r_{ij} \leq r_c, \quad (1)$$

where

$$C = \left(\frac{\lambda_{ij}^r}{\lambda_{ij}^r - \lambda_{ij}^a} \right) \left(\frac{\lambda_{ij}^r}{\lambda_{ij}^a} \right)^{\frac{\lambda_{ij}^a}{\lambda_{ij}^r - \lambda_{ij}^a}}. \quad (2)$$

i and j are the bead types, σ_{ij} indicates the effective bead size, and ϵ_{ij} is the interaction strength between any beads of type i and j . $\lambda_{ij}^a = 6$ and λ_{ij}^r are Mie potential parameters, while r_{ij} is the distance between two CG beads. Units are chosen for the length, σ , energy, ϵ , mass, m , and time τ , which in real units would correspond to: $\sigma = 0.43635$ nm, $\epsilon/k_B = 492$ K, $m = 44.0521$ amu and $\tau = \sigma(m/\epsilon)^{0.5} = 1.4062$ ps. All simulations are carried out in the NVT ensemble by using the Nosé-Hoover thermostat as implemented in the LAMMPS package⁸⁰ with an integration time-step $\delta t = 0.005 \tau$. Our simulations took place at room temperature ($T = 25$ °C), which in the simulation units corresponds to $T = 0.6057 \epsilon/k_B$. Finally, a universal cutoff for all nonbonded (Mie) interactions is set to $r_c = 4.583 \sigma$.

We have considered surfactants of type CiEj, such as C10E8 and C10E4 (Figs 2b, c) and a trisiloxane surfactant.^{4,48–51,67–69} In the case of CiEj surfactants, a hydrophobic alkane CG ‘C’ bead represents a $-\text{CH}_2 - \text{CH}_2 -$

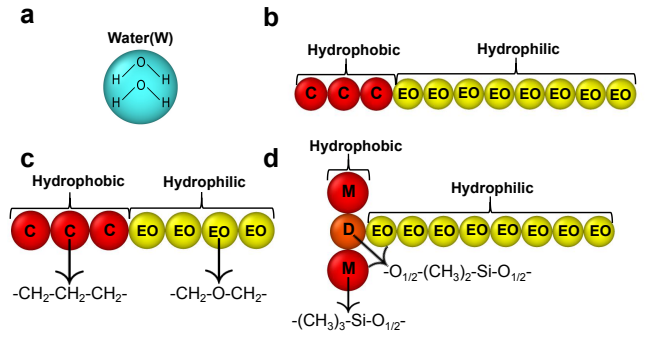


Fig. 2 Coarse-grained representation of water and surfactant molecules. Surfactant’s hydrophobic beads are shown in red, while the hydrophilic parts of the surfactant are in yellow. A cyan bead corresponds to two water molecules (a). C10E8 (b), C10E4 (c), and Silwet-L77 (d) CG surfactant models.

Table 1 Summary of Mie interaction parameters (Eq. 1). $\lambda_{ij}^a = 6$.

$i-j$	$\sigma_{ij} [\sigma]$	$\epsilon_{ij} [\epsilon/k_B]$	λ_{ij}^r
W-W	0.8584	0.8129	8.00
W-C	0.9292	0.5081	10.75
W-EO	0.8946	0.9756	11.94
W-M	1.0491	0.8132	13.72
W-D	0.9643	0.6311	10.38
C-C	1.0000	0.7000	15.00
C-EO	0.9653	0.7154	16.86
M-M	1.2398	0.8998	26.00
M-D	1.1550	0.7114	18.83
M-EO	1.0853	0.8262	22.18
D-D	1.0702	0.5081	13.90
D-EO	1.0004	0.6355	16.21
EO-EO	0.9307	0.8067	19.00

$\text{CH}_2 -$ group of atoms, while a hydrophilic CG ‘EO’ bead represents an oxyethylene group $-\text{CH}_2 - \text{O} - \text{CH}_2$. Silwet-L77 (Fig. 2d) is also considered as a trisiloxane surfactant with the same number of beads as in the case of C10E8, but different hydrophobic chemical units and architecture, where M type beads represent a chemical group $(-\text{CH}_3)_3 - \text{Si} - \text{O}_{1/2}$ and D type $\text{O}_{1/2} - (\text{CH}_3)_2 - \text{Si} - \text{O}_{1/2}$. Finally, a water CG ‘W’ bead corresponds to two water molecules (Fig. 2a). The nonbonded interaction parameters between the above chemical groups, which can be used in practice to simulate a wide range of surfactants with different molecular architecture are reported in Table 1, while the mass of each CG bead is documented in Table 2.

To tether beads together in the case of surfactant chains, a bond potential is required, which in the case of this model is harmonic, *i.e.*,

$$V(r_{ij}) = 0.5k(r_{ij} - \sigma_{ij})^2 \quad (3)$$

Table 2 Mass of the CG beads.

Bead Type	Mass [m]
W	0.8179
C	0.9552
EO	1.0000
M	1.8588
D	1.6833

where the harmonic constant $k = 295.33 \text{ } \epsilon/\sigma^2$. Moreover, EO beads experience a harmonic angle potential,

$$V_{\theta}(\theta_{ijk}) = 0.5k_{\theta}(\theta_{ijk} - \theta_0)^2, \quad (4)$$

where θ_{ijk} is the angle between consecutive beads i, j and k (here, i, j, k indicate the order of EO beads instead of bead type), $k_{\theta} = 4.32 \text{ } \epsilon/\text{rad}^2$, and $\theta_0 = 2.75 \text{ rad}$ is the equilibrium angle. Further discussion on the model can be found in previous studies.^{67–69}

To prepare the initial configuration of each system, individual droplets were first equilibrated in the NVT ensemble. The total number of beads in the simulations was 10^5 per initial droplet, with approximately 5% evaporation into the gas. Droplet diameters were $\sim 53\sigma$, which is about 23 nm, similar to that of several previous studies.^{9,45} Careful consideration was given not only to observing the energy of the system, but, also, making sure that the distribution of surfactant clusters has reached a dynamic equilibrium and that each of them was able to diffuse a distance many times its size. After equilibration of the individual droplets, the volume of the simulation box was doubled and the two droplets (and the surrounding gas) were placed next to each other as shown in Fig. 1a. In this way, roughly the same thermodynamic conditions are maintained and further evaporation that would reduce the number of water molecules of the droplets is avoided. The final size of the simulation box is also chosen large enough to avoid the interaction of mirror images of the droplets over the periodic boundary conditions. Figure 1 illustrates typical snapshots at different stages during coalescence for cases below and above CAC. For our study, we have considered a range of different surfactant concentrations up to about $6 \times \text{CAC}$, which cover the relevant span of phenomena. A summary of the mean values of various properties for our systems is given in Table 3. We can see that increasing surfactant concentration slightly increases the size of the droplet. Also, note that the CAC in the case of Silwet-L77 in terms of wt% is almost double that of C10E4 and C10E8 surfactants.

To obtain reliable estimates of the bridge growth dynamics and the mass transport mechanism, snapshots of the system are made frequently (every 250 MD time steps) for

Table 3 Properties of individual droplets (equilibrium)

Concentration (wt%)	Diameter (σ)	Water Beads*	# Molecules
C10E4			
6.25	53.08	90466.09	714
12.37	53.02	85496.45	1429
24.18	53.62	75572.27	2857
35.48	54.14	65746.73	4286
46.02	54.63	55966.55	5714
CAC $\approx 7.5 \text{ wt\%}$			
C10E8			
6.25	52.74	90519.09	455
12.37	52.98	85500.09	909
24.18	53.40	75722.36	1818
35.48	53.91	65862.36	2727
46.02	54.33	56488.91	3636
CAC $\approx 7.5 \text{ wt\%}$			
Silwet-L77			
7.6	52.62	90438.45	455
14.8	53.01	85574.64	909
28.2	53.89	75786.36	1818
40.3	54.78	66312.82	2727
51.2	55.71	56787.91	3636
CAC $\approx 16.23 \text{ wt\%}$			

* Indicates the average number of water beads.

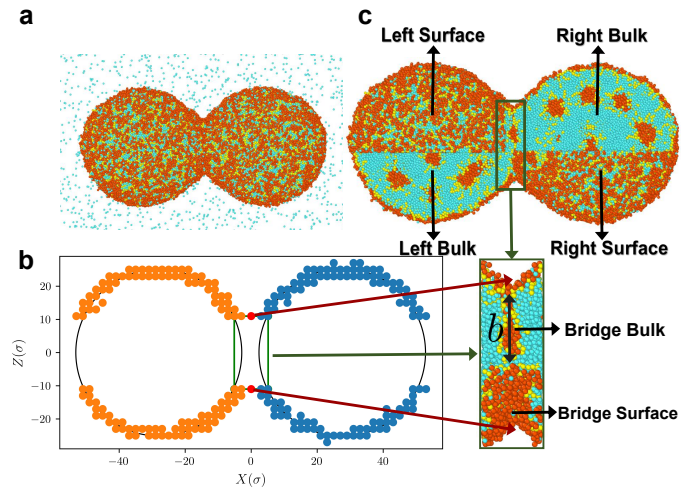


Fig. 3 Bridge analysis and domains for analysing the mass transport mechanism. Six different regions for the position of the molecules within the droplets are considered, namely, bridge bulk and surface, left and right surface and bulk. (a) A snapshot obtained by the MD simulation with a clearly developed bridge length. (b) Analysis of an $X-Z$ projection for identifying the bridge based on the method described in Sec. 3. (c) Different regions of the droplets considered for analysing the mass transport mechanism of surfactants between these regions (see ESI for further details).

the initial 4×10^5 MD time steps, and cluster analysis is performed to identify the beads belonging to the liquid phase (droplets), which is used for our properties analysis. The bridge region is chosen to be a slab with a width in the

X (approach) direction that is calculated for each configuration. In particular, the left and right limits of the slab are determined by analysing the grid points on the $X - Z$ plane at position $Y = 0$ according to the procedure shown in Fig. 3b. We fit a circle around each droplet and note the surface grid positions at the central $X = 0$ position, shown by the red points in Fig. 3b. Horizontal lines are drawn in the X direction passing through these red points to touch the fitted circles, thus defining the rectangle in green. The vertical sides of the rectangle give the limits of the bridge slab in the X direction, and its width. All molecules with centres having X coordinates inside these limits are labelled as belonging to the bridge in a given snapshot. On the other hand, the bridge radius b shown in Figs 1c and 3 is calculated using the distances between extrema of the positions of the beads belonging to the grids located at $X = 0$. That is this distance is first calculated separately for the Z coordinate to give a distance $2b_Z$, and then for the Y coordinate to give $2b_Y$. The final bridge radius estimate is then given by $b = (b_Z + b_Y)/2$.

We also describe the mass transport mechanism by tracking each surfactant molecule during the coalescence and then identifying the probability of adsorption of each molecule to different regions in the liquid phase, namely the left and right LG surfaces and the bulk, and the surface and interior of the bridge (Fig. 3b, c). Further discussion and details on the calculation of probabilities related to the mass transport mechanism can be found in the Electronic Supplementary Information (ESI). Finally, we have calculated the density profiles of the water and surfactant molecules during coalescence, the flow field at different times, as well as the approach distance and velocity of approach of the droplets and their asphericity, for which further details are discussed in the ESI.

4 Results and Discussion

4.1 Coalescence mechanism

The initial stage of droplets' coalescence manifests itself via their pinching as illustrated by the snapshots of Fig. 4 and movies in the ESI. In this early stage of the phenomenon, a previous study on coalescence with pure water droplets has shown via all-atom MD that multiple bridges form on the surface of the droplets and the overall radius of the affected region grows linearly over time.⁹ Here, we rather see that the droplet pinching initially involves only the surfactant molecules at the droplets' surfaces, particularly when the surfactant concentration is higher. Here and in those previous results the size of the droplets are about the same. Fig. 4 illustrates the single pinching of the droplets based on our model, whereby hydrophobic parts of the surfactants come together forming aggregates, while water

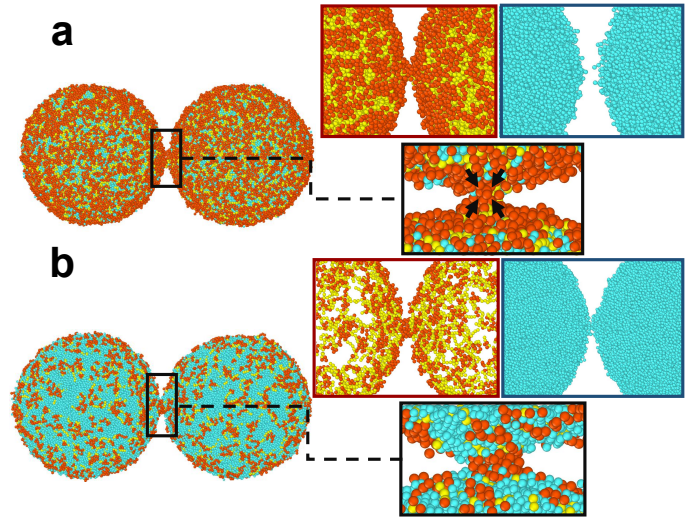


Fig. 4 Pinching of droplets with C10E4 surfactant in the TR for concentration above (a, 35.4 wt%) and below (b, 6.25 wt%) CAC. For each case, a magnified view of the initial bridge formation is shown, as well as the distribution of surfactant (hydrophobic beads in red and hydrophilic in yellow colour) and water molecules (cyan colour). (a) $t = t_c + 8.75 \tau$, (b) $t = t_c + 8.75 \tau$.

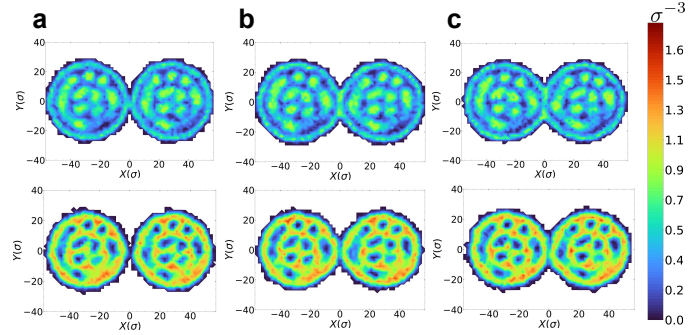


Fig. 5 Density profiles of surfactant beads, C10E4 (46.2 wt%) (upper row) and water beads (lower row) on the mid plane (width of 6σ) at different stages after the time t_c at which a permanent contact between the droplets is established (a) $t = t_c \tau$, (b) $t = t_c + 71.25 \tau$, (c) $t = t_c + 98.75 \tau$.

molecules remain further from the pinching point (Fig. 4). By inspecting the density profile of the droplets during coalescence and considering a cross-section on the $X - Y$ plane passing through the centre of mass of the droplets for high-concentration droplets, we can better highlight the aggregates at the cross-section (Fig. 5). One can observe that the water density between the droplets is negligible (the grid used for the calculation of the density profile does not resolve the bead size), in contrast to the density of surfactant. Therefore, the latter is solely responsible for the droplet pinching. At later times and when the bridge has developed past the very initial pinching stage, water molecules become part of the bridge (Fig. 5b). However, the bridge

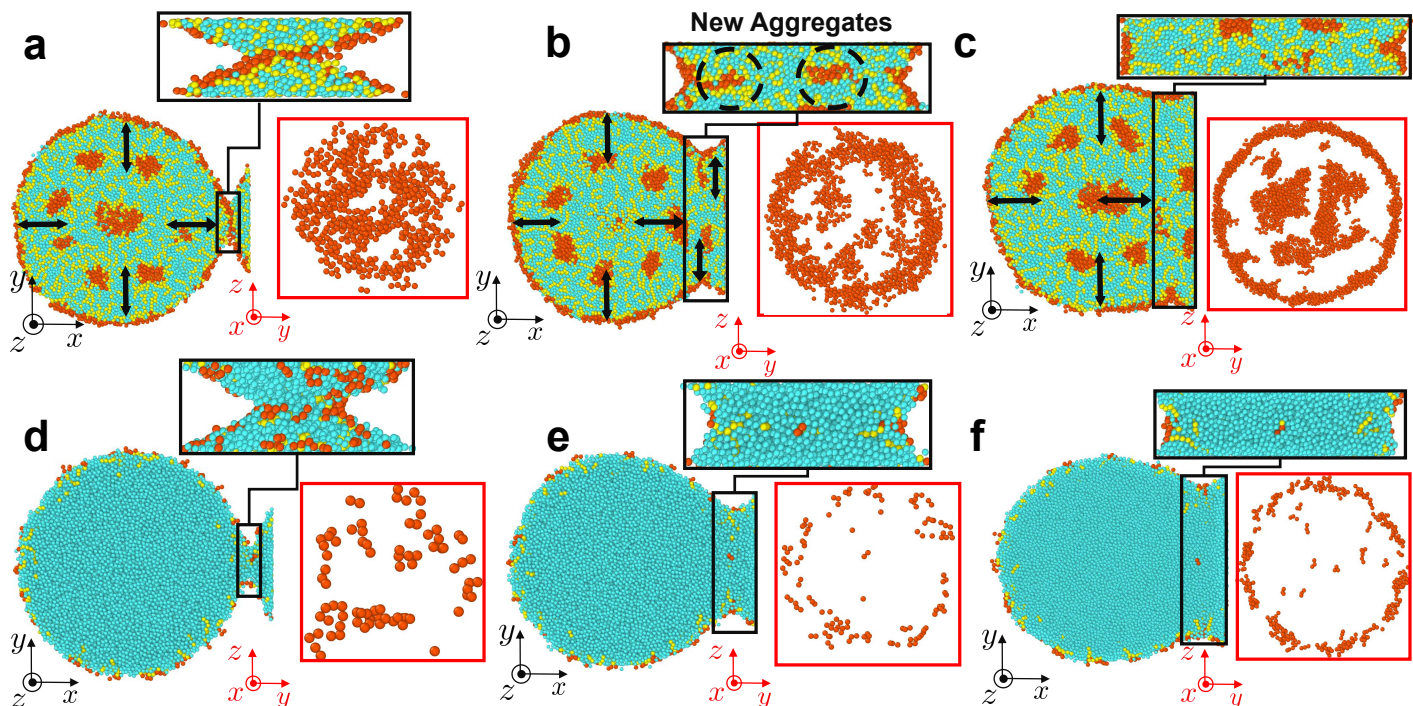


Fig. 6 Mass transport mechanism of surfactant (C10E8) during the coalescence process, for concentrations above (upper panel) and below (lower panel) CAC. The size of the arrows reflects the probabilities associated with surfactant transport to the different droplet areas (see Table S4 of the ESI for further details). Above the CAC (a–c, 46.2 wt%) snapshots were obtained at times (a) $t_c + 22.5 \tau$, (b) $t_c + 172.5 \tau$, (c) $t_c + 480.0 \tau$ while below the CAC (d–f, 6.2 wt%) times shown are (d) $t_c + 25.0 \tau$, (e) $t_c + 66.3 \tau$, (f) $t_c + 116.3 \tau$, soon after the end of the thermal regime (a,d), the development of the bridge and the formation of new aggregates (b) or surfactant monomers remaining in the bridge region (e), and the full development of the bridge (c, f). Magnified views of the bridge region and its cross-section (showing only surfactant hydrophobic beads in the bridge region, red) are attached above and to the right of the snapshots, respectively. Figure S4 in the ESI illustrates results for the C10E4 surfactant.

region is still dominated by the presence of surfactant, with surfactant density values similar to those inside aggregates. It is notable that surfactant continues to be present in the bridge in significant amounts even at later stages of coalescence, when the bridge has been almost fully developed (Fig. 5c). The reasons for this will become more apparent when further details on the surfactant mass transport are unveiled.

After the initial droplet pinching (Fig 4), the contact between the droplet persists and the growth of the bridge, which manifests by the large change in curvature at the surface, takes place as shown in Fig. 6. Moreover, we analysed the surfactant mass transport mechanism during coalescence, and the main adsorption processes of surfactant were monitored. These processes are described by the probabilities of surfactant remaining at a particular region or moving between the different regions shown in Fig. 3c during coalescence. These are documented in the ESI for all surfactant types and concentrations considered in our study. On the basis of these probabilities we have indicated by arrows the main surfactant movements (Fig. 6). In particular, the concentration of surfactant is high at the

initial contact of the droplets due to the preexisting surfactant at the droplet surfaces (Fig. 6a, d), which becomes trapped in between the droplets. As the bridge gradually grows, we observe that most of the surfactant, which was initially on the surfaces of the droplets, preferably moves towards the surface of the bridge, which is energetically more favourable. However, the bridge surface has limited place for accommodating all surfactant from the initial LG surfaces of the droplets, since in this area between the droplets the surface excess concentration is doubled at the initial approach. As a result, some surfactant remains in the bulk and forms new aggregates, which is most clearly seen in the case of higher surfactant concentrations (Fig. 6b, c and Figs. S1–S3 and movie in the ESI). In contrast, when the concentration is lower than CAC, the bridge surface is able to accommodate surfactant molecules that existed on the LG surfaces before the coalescence (see Tables S1–S3 for detailed surfactant counts).

We observe that most of the surfactant activity takes place in the bridge area and that the dominant process is transport towards the bridge surface. We do not see any clear evidence of Marangoni flow in the studied system,

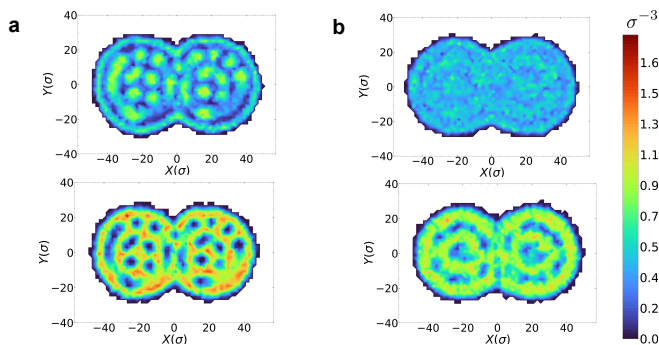


Fig. 7 Density profiles of a $X-Y$ cross-section (X and Y are the coordinates of the centre point of each grid voxel) passing through the centre of mass of the droplets with (a) C10E4 (46.2 wt%) $t = t_c + 288.75 \tau$ and (b) Silwet-L77 (51.2 wt%), $t = t_c + 437.50 \tau$. Upper panels show the number density of the surfactant beads, lower panels of the water.

possibly due to there not being enough space or time for it to develop. By analysing our data, we have verified that the qualitative features of the mass transport mechanism are independent of the surfactant type or concentration, while the largest quantitative differences were seen in the case of Silwet-L77. In particular, Silwet-L77 tends to form a larger number of aggregates but their overall density is lower than that of the C10E4 and C10E8 surfactants, which also implies that higher quantities of water molecules are found among surfactant in the case of droplets with Silwet-L77. To illustrate these effects, the density profiles of droplets with either C10E4 or Silwet-L77 with high surfactant concentration are plotted in Fig. 7. Finally, in terms of the mass transport (Table S4 in the ESI contains details), we find that Silwet-L77 have a higher tendency to move towards the surface of the bridge in comparison with C10E4 and C10E8 surfactants, which is in line with previous observations in systems with surfactant-laden droplets.⁶⁹ In turn, this results in the formation of fewer aggregates in the bridge in the case of droplets with Silwet-L77 surfactant.

4.2 Water flow

In a previous study,⁴⁵ we have shown that the coalescence of water droplets is characterised by intense internal flow variations during the thermal regime, which attenuate with the increase of surfactant concentration. Figure 8 illustrates the flow of water in the case of water droplets and those with surfactant after the initial thermal regime and at the initial stages of the power-law (IR) regime. Firstly, as expected, the data suggest that there is an increased water flow toward the bridge (red colour) throughout the coalescence process. This is particularly visible in the bulk in

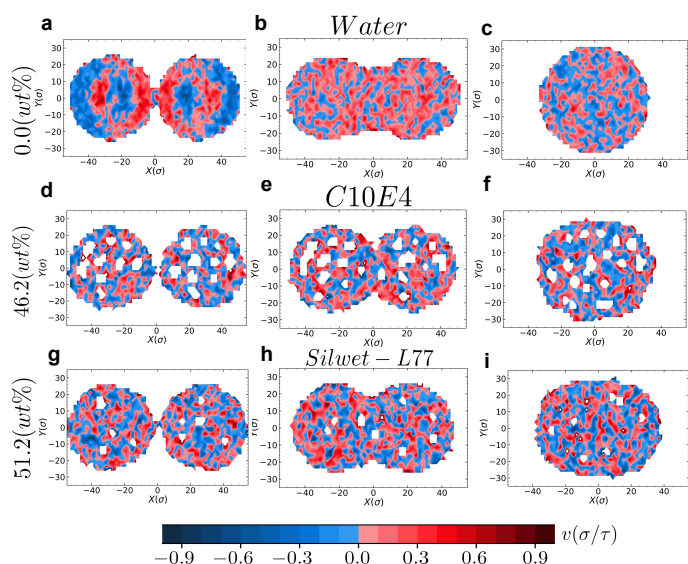


Fig. 8 Flow field of water inside the droplets for the case without surfactant (a–c), with C10E4 (46.2 wt%, d–f), and with Silwet-L77 (51.2 wt%, g–i) surfactant. Cross-sections through the centre of mass are shown. Red reflects the intensity of flow motion (only water) toward the bridge X component of velocity v , blue away from the bridge. The averaged data of red and blue grids indicating the total flow towards the bridge and away of it in the droplets and in the bridge region are reported in the ESI and discussed further in the main text. Note that the white space between the water areas (e.g. in the bridge) includes surfactant aggregates and surfactant on the surface. The snapshots were obtained at times (a, d, g) t_c (b) $t_c + 90.75 \tau$, (c) $t_c + 275.25 \tau$, (e) $t_c + 183.75 \tau$, (f) $t_c + 2446 \tau$, (h) $t_c + 425 \tau$, and (i) $t_c + 2437.5 \tau$.

the IR phase, as can be better seen in data included in Tables S6–S8 in the ESI. These are separately averaged for the red and the blue grids and concern the pure water and surfactant-laden droplets at high concentration. Moreover, surfactant attenuates the free flow of water molecules toward the bridge, because it reduces the surface tension at the droplets' LG surface and moreover forms aggregates in the bulk that hinder the flow directly. The formation of aggregates at the pinching point is also seen, which manifests by the empty spots in the flow field of Fig. 8. These observations are valid for all of the different surfactants studied here and for the whole range of concentrations above CAC.

4.3 Bridge Growth

The growth rate of the bridge radius, b , is a key parameter that characterises the dynamics of the coalescence process. From a fluid dynamics perspective, the VR and IR have mainly been proposed, where the former manifests itself through a linear dependence on time, $b \sim t$, while the latter is described by a slower power-law dependence, namely $b \sim t^\beta$ ^{10,52,55,81} with expected $\beta \approx \frac{1}{2}$. In addition, all-atom

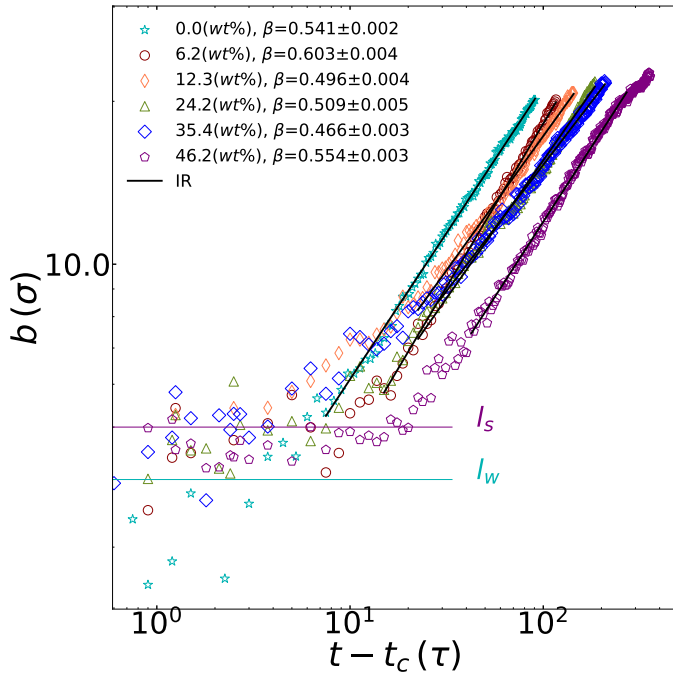


Fig. 9 Bridge length b as a function of time from the first contact of the droplets at t_c for different concentrations of C10E4 surfactant, as indicated. Power-law fits $\sim t^\beta$ are shown, labeled “IR”. l_s is the thermal length in the case of surfactant-laden droplets above CAC, while l_w is the thermal length in the case of pure water droplets.

molecular dynamics have identified a thermal regime at the very early stage of coalescence, which persists over the length scale l_T as mentioned in Sec. 1.⁹ Well beyond this length, the hydrodynamic description is considered valid. In view of the importance of b in describing the dynamics of coalescence and the various scenarios discussed thus far in the literature, we have embarked here on investigating the time evolution of b for a range of different surfactants and concentrations. Figure 9 presents results for droplets with C10E4 surfactant at different concentrations, both below and above the CAC. In Fig. S6 in the ESI, results for other surfactants and concentrations are shown. Overall, our model captures two different coalescence regimes, namely an initial TR and a subsequent power-law regime characterised by power law exponents β in the range 0.46 – 0.71, mean $\beta = 0.57$ close to those predicted by IR scaling. We observe different exponents for different surfactant concentration, with more or less random variation from case to case, which may be due to finite size effects and different internal aggregate configurations. Prefactors generally decrease with growing surfactant concentration, leading to a slowdown of growth. Hence, as in the case of all-atom water simulation,⁹ our CG model is also confirming the existence of a TR and an inertial-like power-law regime. The

TR persists over a time $\mathcal{O}(10 \tau)$ during which the length of the bridge is well described by the length l_T both for the pure and the surfactant-laden droplets. In Fig. 10, we compare the bridge growth for three different surfactants below and well above CAC to each other and pure water. Differences in the surface tension above CAC for the different surfactants are generally expected to be small, and our results for $b(t)$ also differ a little, which agrees with the expectation that bridge size in this regime is determined by the thermal length $l_T \propto \gamma^{-1/4}$.

Following the TR, we observe the transition to the power-law regime. The time for the transition to occur is longer when droplets have a higher surfactant concentration. The power-law regime is characterised by exponents close and generally above 0.5. The mean over all cases is $\beta = 0.57$ and standard deviation 0.06, while the reference pure water case gives $\beta = 0.541$. It is also clearly seen that adding surfactant will lead to slower dynamics overall, regardless of exponent variability, as well as a delay in the start of the bridge growth — see ESI Fig. S5. We can also see a trend that C10E8 clearly has higher β exponent than pure water and than C10E4 (Compare Fig. S6 in the ESI with Fig. 9). Otherwise, the main variation lies in the reduction of the growth prefactor as surfactant concentration grows, as can be seen by the progressive shifting of the evolution to the right in the logarithmic plots of Figs. 9, 10, and ESI Fig. S6. This trend is broadly similar for all surfactants that we studied, with the addition that Silwet-L77 displayed a significantly slower growth in all respects, and in particular lower maximum velocity (see ESI, Figs. S7–S8).

4.4 Velocity of approach and asphericity

A complementary measure of the coalescence dynamics is obtained by monitoring the total length of the droplets in the X direction, whence the velocity of approach $u = \dot{X}$ can be obtained.^{25,82} Data for droplets with C10E4 surfactant are presented in Fig. 11, and show that the fastest approach takes place in the middle of the process at a time about 150τ , which is similar for different surfactants. Although the exponents β of the bridge radius are roughly similar for all cases, we observe that the droplets with surfactant consistently exhibit a smaller maximum speed. Moreover, the process is shorter in time in the case of pure water droplets. A different behaviour appears well above CAC (e.g. four times above), when the process becomes significantly slower, sometimes rather suddenly. A conjecture is that this is due to increased internal rigidity of the aggregates present in the bulk. Monitoring the ratio of droplet radius to bridge radius $L_y/l_{br} \approx R_0/b$ one finds that max-

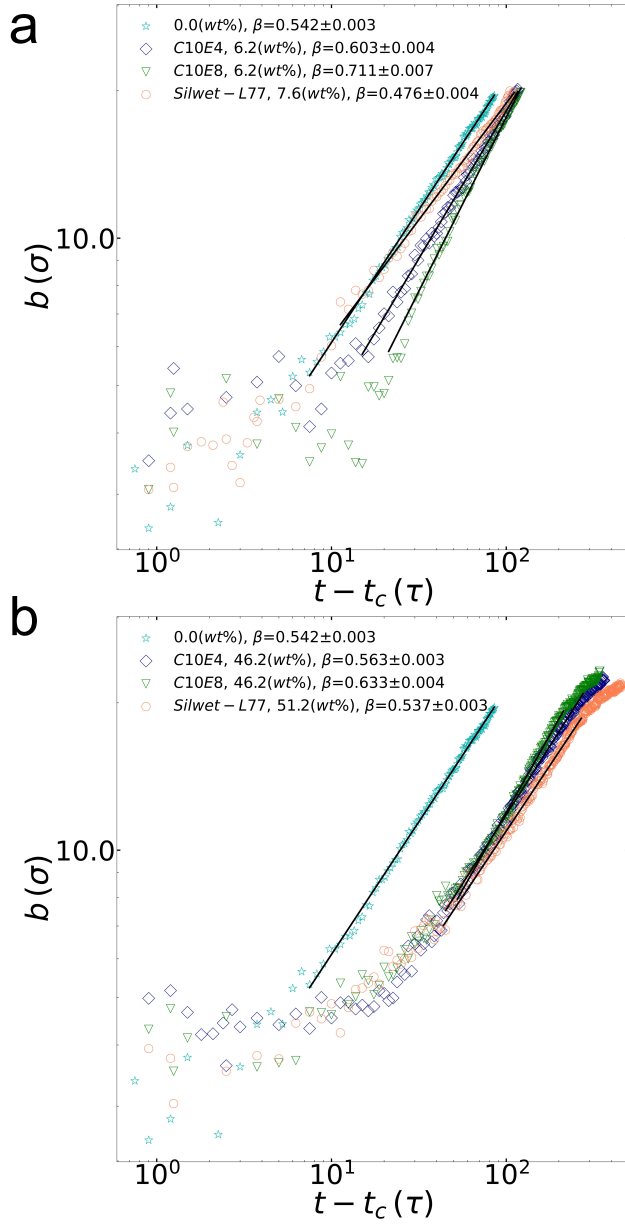


Fig. 10 Comparison of bridge radius growth $b(t)$ for different surfactants, below (a) and significantly above (b) CAC. Power-law fits $\sim t^\beta$ are shown, for times counted from the first contact of the droplets at t_c .

imum coalescence velocity occurs for very broad bridges $L_y/l_{br} \approx 1.2$ when the surfactant concentration is low but earlier and for much smaller bridge size $L_y/l_{br} \approx 1.8$ when well above CAC. This would be consistent with the conjecture that a major slowdown occurs once significant internal rearrangements, as necessitated by a broad bridge in high concentrations, become necessary. Further results for different surfactants and comparative plots are shown in the ESI (Figs S7 and S8).

Monitoring the asphericity of the two coalescing droplets

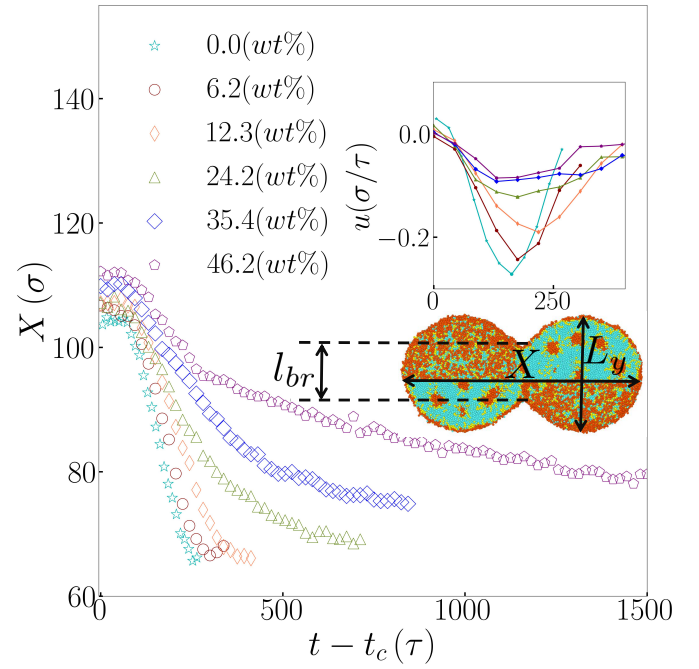


Fig. 11 System length, X , in the coalescence direction for different concentrations of C10E4. The inset shows the instantaneous velocity of approach $u = dX/dt$. The maximum speed occurs at droplet-to-bridge width ratios of $L_y/l_{br}=1.22$ (0.0 wt%), 1.22 (6.2 wt%), 1.30 (12.3 wt%), 1.40 (24.2 wt%), 1.80 (35.4 wt%), 1.80 (46.2 wt%).

(Figs S9 and S10 in the ESI), as a complimentary measure to monitor the lateral changes in the dimensions of the system, we can observe that this generally follows the behaviour of the velocity of approach. Pure water droplets complete the coalescing process obtaining the final spherical shape much faster than in the case of droplets with surfactant. As with approach velocity and system size, we see a change in behaviour when surfactant concentration increases, but the change is gradual and does not occur at the CAC but well above.

5 Conclusions

In this study, we have analysed various macroscopic and microscopic properties of droplets laden with surfactant and unveiled the surfactant mass transport mechanism during the process for different surfactants and a range of concentrations. We have demonstrated that the underlying mechanisms and flow patterns of coalescence are universal, qualitatively and often quantitatively independent of the type of surfactant. Particular differences between Silwet-L77 and CiEj surfactants have been noted in the bridge dynamics for concentrations below the CAC. We have also observed that water molecules are not part of the initial pinching process of coalescence at larger (above CAC) sur-

factant concentration, which is driven by surfactant aggregation at the droplet's surface.

Other features include the engulfment of part of the initial contact surface inside the forming bridge, the existence of an initial thermal regime, followed by a later power-law growth of the bridge radius with power exponents close to $\frac{1}{2}$, as expected in the inertial regime. We saw no evidence of an intermediate viscous regime. One possibility is that the droplets, despite being large computationally, were still too small for the VR to emerge out of the thermal regime before the IR is activated. Coalescence also universally becomes slower as surfactant concentration grows, and we see evidence of the appearance of a further slowdown with different qualities for several times the critical concentration, using several different indicators. We conjecture that this is due to the appearance of greater internal stiffness caused by closely-packed surfactant aggregates in the bulk. The range of concentrations studied here reflects the need in practical applications where surfactant concentration is usually above the CAC.⁸³ We anticipate that our results demonstrate the mechanisms of a fundamental process in nature and technological applications, which remain universal.

Conflicts of interest

There are no conflicts to declare

Acknowledgements

This research has been supported by the National Science Centre, Poland, under grant No. 2019/34/E/ST3/00232. We gratefully acknowledge Polish high-performance computing infrastructure PLGrid (HPC Centers: ACK Cyfronet AGH) for providing computer facilities and support within computational grant no. PLG/2022/015747.

Notes and references

- 1 S. Feng, L. Yi, L. Zhao-Miao, C. Ren-Tuo and W. Gui-Ren, *Chinese J. Anal. Chem.*, 2015, **43**, 1942–1954.
- 2 J.-C. Baret, *Lab Chip*, 2012, **12**, 422–433.
- 3 W. Ristenpart, P. McCalla, R. Roy and H. Stone, *Phys. Rev. Lett.*, 2006, **97**, 064501.
- 4 P. E. Theodorakis, E. A. Müller, R. V. Craster and O. K. Matar, *Curr. Opin. Colloid Interface Sci.*, 2014, **19**, 283–289.
- 5 P. E. Theodorakis, E. R. Smith, R. V. Craster, E. A. Müller and O. K. Matar, *Fluids*, 2019, **4**, 176.
- 6 J. D. Paulsen, R. Carmigniani, A. Kannan, J. C. Burton and S. R. Nagel, *Nat. Commun.*, 2014, **5**, 3182.
- 7 Y. Yoon, F. Baldessari, H. D. Cenicerros and L. G. Leal, *Phys. Fluids*, 2007, **19**, 102102.
- 8 M. I. Khodabocus, M. Sellier and V. Nock, *Adv. Math. Phys.*, 2018, **2018**,.
- 9 S. Perumanath, M. K. Borg, M. V. Chubynsky, J. E. Sprittles and J. M. Reese, *Phys. Rev. Lett.*, 2019, **122**, 104501.
- 10 J. Eggers, J. R. Lister and H. A. Stone, *J. Fluid Mech.*, 1999, **401**, 293–310.
- 11 D. G. Aarts, H. N. Lekkerkerker, H. Guo, G. H. Wegdam and D. Bonn, *Phys. Rev. Lett.*, 2005, **95**, 164503.
- 12 J. Sprittles and Y. Shikhmurzaev, *Phys. Fluids*, 2012, **24**, 122105.
- 13 M. Dudek, D. Fernandes, E. Helno Herø and G. Øye, *Colloids Surf. A: Physicochem. Eng. Asp.*, 2020, **586**, 124265.
- 14 M. M. Rahman, W. Lee, A. Iyer and S. J. Williams, *Phys. Fluids*, 2019, **31**, 012104.
- 15 J. D. Berry and R. R. Dagastine, *J. Colloid Interface Sci.*, 2017, **487**, 513–522.
- 16 P. M. Somwanshi, K. Muralidhar and S. Khandekar, *Phys. Fluids*, 2018, **30**, 092103.
- 17 P. K. Kirar, K. Alvarenga, P. Kolhe, G. Biswas and K. Chandra Sahu, *Phys. Fluids*, 2020, **32**, 052103.
- 18 S. Bayani, Y. Tabe, Y. T. Kang, S. H. Lee and C. K. Choi, *J. Flow Vis. Image Process.*, 2018, **25**, 191–205.
- 19 M. Brik, S. Harmand and I. Zaaroura, *Colloids Surf. A: Physicochem. Eng. Asp.*, 2021, **629**, 127429.
- 20 C. R. Anthony, M. T. Harris and O. A. Basaran, *Phys. Rev. Fluids*, 2020, **5**, 033608.
- 21 V. R. Kern, T. Sæter and A. Carlson, *Phys. Rev. Fluids*, 2022, **7**, L081601.
- 22 M. Heinen, M. Hoffmann, F. Diewald, S. Seckler, K. Langenbach and J. Vrabec, *Phys. Fluids*, 2022, **34**, 042006.
- 23 M. Geri, B. Keshavarz, G. H. McKinley and J. W. M. Bush, *J. Fluid Mech.*, 2017, **833**, R3.
- 24 M. Abouelsoud and B. Bai, *Phys. Fluids*, 2021, **33**, 063309.
- 25 S. Arbabi and P. E. Theodorakis, *Macromol. Theory Simul.*, 2023, **32**, 2300017.
- 26 P. J. Dekker, M. A. Hack, W. Tewes, C. Datt, A. Bouillant and J. H. Snoeijer, *Phys. Rev. Lett.*, 2022, **128**, 028004.
- 27 E. Calvo, E. de Malmazet, F. Risso and O. Masbernat, *Ind. Eng. Chem. Res.*, 2019, **58**, 15573–15587.
- 28 V. S. Sivasankar, D. R. Hines and S. Das, *Langmuir*, 2022, **38**, 14084–14096.
- 29 M. R. Otazo, R. Ward, G. Gillies, R. S. Osborne, M. Golding and M. A. K. Williams, *Soft Matter*, 2019, **15**, 6383–6391.
- 30 C. Vannozzi, *Phys. Fluids*, 2019, **31**, 082112.

- 31 L. Y. Yeo, O. K. Matar, E. S. P. de Ortiz and G. F. Hewitt, *J. Colloid Interface Sci.*, 2003, **257**, 93–107.
- 32 Y. Hu, D. Pine and L. G. Leal, *Phys. Fluids*, 2000, **12**, 484–489.
- 33 A. Mansouri, H. Arabnejad and R. Mohan, Fluids Engineering Division Summer Meeting, 2014, p. V01AT05A006.
- 34 L. Duchemin, J. Eggers and C. Josserand, *J. Fluid Mech.*, 2003, **487**, 167–178.
- 35 G. Karapetsas, R. V. Craster and O. K. Matar, *J. Fluid Mech.*, 2011, **670**, 5–37.
- 36 E. Nowak, N. M. Kovalchuk, Z. Che and M. J. Simmons, *Colloids Surf. A Physicochem. Eng. Asp.*, 2016, **505**, 124–131.
- 37 S. Narayan, A. E. Metaxas, R. Bachnak, T. Neumiller and C. S. Dutcher, *Curr. Opin. Colloid Interface Sci.*, 2020, **50**, 101385.
- 38 E. Nowak, Z. Xie, N. M. Kovalchuk, O. K. Matar and M. J. Simmons, *Soft Matter*, 2017, **13**, 4616–4628.
- 39 L. Leal, *Phys. Fluids*, 2004, **16**, 1833–1851.
- 40 N. I. Politova, S. Tcholakova, S. Tsibranska, N. D. Denkov and K. Muelheims, *Colloids Surf. A: Physicochem. Eng. Asp.*, 2017, **531**, 32–39.
- 41 T. Dong, W. H. Weheliye, P. Chausset and P. Angeli, *Phys. Fluids*, 2017, **29**, 102101.
- 42 T. Dong, W. H. Weheliye and P. Angeli, *Phys. Fluids*, 2019, **31**, 012106.
- 43 W. H. Weheliye, T. Dong and P. Angeli, *Chem. Eng. Sci.*, 2017, **161**, 215–227.
- 44 N. M. Kovalchuk, M. Reichow, T. Frommweiler, D. Vigolo and M. J. H. Simmons, *Langmuir*, 2019, **35**, 9184–9193.
- 45 S. Arbabi, P. Deuar, M. Denys, R. Bennacer, Z. Che and P. E. Theodorakis, *Phys. Fluids*, 2023, **35**, 063329.
- 46 S. Li, X. Zhang, W. Dong and W. Wang, *Langmuir*, 2008, **24**, 9344–9353.
- 47 H. A. Ritacco, F. Ortega, R. G. Rubio, N. Ivanova and V. M. Starov, *Colloids Surf. A: Physicochem. Eng. Asp.*, 2010, **365**, 199–203.
- 48 H. A. Ritacco, V. B. Fainerman, F. Ortega, R. G. Rubio, N. Ivanova and V. M. Starov, *Colloids Surf. A: Physicochem. Eng. Asp.*, 2010, **365**, 204–209.
- 49 N. Ivanova, V. Starov, R. Rubio, H. Ritacco, N. Hilal and D. Johnson, *Colloids Surf. A: Physicochem. Eng. Asp.*, 2010, **354**, 143–148.
- 50 N. Ivanova, Z. Zhantenova and V. Starov, *Colloids Surf. A: Physicochem. Eng. Asp.*, 2012, **413**, 307–313.
- 51 N. Ivanova, V. Starov, D. Johnson, N. Hilal and R. Rubio, *Langmuir*, 2009, **25**, 3564–3570.
- 52 J. D. Paulsen, *Phys. Rev. E*, 2013, **88**, 063010.
- 53 M. Gross, I. Steinbach, D. Raabe and F. Varnik, *Phys. Fluids*, 2013, **25**, 052101.
- 54 S. Thoroddsen, K. Takehara and T. Etoh, *J. Fluid Mech.*, 2005, **527**, 85–114.
- 55 J. D. Paulsen, J. C. Burton, S. R. Nagel, S. Appathurai, M. T. Harris and O. A. Basaran, *Proc. Natl. Acad. Sci. U.S.A.*, 2012, **109**, 6857–6861.
- 56 H. Xu, T. Wang and Z. Che, *J. Colloid Interface Sci.*, 2022, **628**, 869–877.
- 57 G. Soligo, A. Roccon and A. Soldati, *J. Comput. Phys.*, 2019, **376**, 1292–1311.
- 58 T. C. Botti, A. Hutin, E. Quintella and M. S. Carvalho, *Soft Matter*, 2022, **18**, 1423–1434.
- 59 C. Constante-Amores, A. Batchvarov, L. Kahouadji, S. Shin, J. Chergui, D. Juric and O. Matar, *J. Fluid Mech.*, 2021, **925**, A15.
- 60 M. Kasmaee, F. Varaminian, P. Khadiv-Parsi and J. Saien, *J. Mol. Liq.*, 2018, **263**, 31–39.
- 61 N. Jaensson and J. Vermant, *Curr. Opin. Colloid Interface Sci.*, 2018, **37**, 136–150.
- 62 I. B. Ivanov, K. D. Danov and P. A. Kralchevsky, *Colloids Surf. A Physicochem. Eng.*, 1999, **152**, 161–182.
- 63 S. Tcholakova, N. D. Denkov and T. Danner, *Langmuir*, 2004, **20**, 7444–7458.
- 64 D. Langevin, *Curr. Opin. Colloid Interface Sci.*, 2019, **44**, 23–31.
- 65 O. D. Velev, T. D. Gurkov and R. P. Borwankar, *J. Colloid Interface Sci.*, 1993, **159**, 497–501.
- 66 V. C. Suja, A. Kar, W. Cates, S. M. Remmert, P. D. Savage and G. G. Fuller, *Proc. Natl. Acad. Sci. U.S.A.*, 2018, **115**, 7919–7924.
- 67 P. E. Theodorakis, E. A. Müller, R. V. Craster and O. K. Matar, *Soft Matter*, 2015, **11**, 9254–9261.
- 68 P. E. Theodorakis, E. A. Müller, R. V. Craster and O. K. Matar, *Langmuir*, 2015, **31**, 2304–2309.
- 69 P. E. Theodorakis, E. R. Smith and Müller, *Colloids Surf. A: Physicochem. Eng. Asp.*, 2019, **581**, 123810.
- 70 W. G. Chapman, K. E. Gubbins, G. Jackson and M. Radosz, *Fluid Phase Equil.*, 1989, **52**, 31–38.
- 71 E. A. Müller and K. E. Gubbins, *Industrial & engineering chemistry research*, 2001, **40**, 2193–2211.
- 72 C. Avendaño, T. Lafitte, A. Galindo, C. S. Adjiman, G. Jackson and E. A. Müller, *J. Phys. Chem B*, 2011, **115**, 11154–11169.
- 73 C. Avendaño, T. Lafitte, A. Galindo, C. S. Adjiman, E. A. Müller and G. Jackson, *J. Phys. Chem B*, 2013, **117**, 2717–2733.
- 74 D. Sergi, G. Scocchi and A. Ortona, *J. Chem. Phys.*, 2012, **137**, 094904.

- 75 E. A. Müller and G. Jackson, *Annu. Rev. Chem. Biomol. Eng.*, 2014, **5**, 405–427.
- 76 T. Lafitte, A. Apostolakou, C. Avendaño, A. Galindo, C. S. Adjiman, E. A. Müller and G. Jackson, *J. Chem. Phys.*, 2013, **139**, 154504.
- 77 O. Lobanova, *PhD thesis*, Imperial College London, 2014.
- 78 O. Lobanova, A. Mejia, G. Jackson and E. A. Müller, *J. Chem. Thermodyn.*, 2016, **93**, 320–336.
- 79 P. Morgado, O. Lobanova, E. A. Müller, G. Jackson, M. Almeida and E. J. Filipe, *Mol. Phys.*, 2016, **114**, 2597–2614.
- 80 A. P. Thompson, H. M. Aktulga, R. Berger, D. S. Bolintineanu, W. M. Brown, P. S. Crozier, P. J. in 't Veld, A. Kohlmeyer, S. G. Moore, T. D. Nguyen, R. Shan, M. J. Stevens, J. Tranchida, C. Trott and S. J. Plimpton, *Comp. Phys. Comm.*, 2022, **271**, 108171.
- 81 J. Frenkel, *J. phys.*, 1945, **9**, 385.
- 82 C. Verdier and M. Brizard, *Rheol. Acta*, 2002, **41**, 514–523.
- 83 I. M. Gonçalves, I. Castro, F. Barbosa, V. Faustino, S. O. Catarino, A. Moita, J. M. Miranda, G. Minas, P. C. Sousa and R. Lima, *Processes*, 2022, **10**, 2698.